Article

Spin-valley Rashba monolayer laser

🔺 Check for updates

Kexiu Rong ⓘ [1], **Xiaoyang Duan**[1], **Bo Wang** ⓘ [2], **Dror Reichenberg**[1],
Assael Cohen ⓘ [3], **Chieh-li Liu**[1], **Pranab K. Mohapatra**[3], **Avinash Patsha** ⓘ [3],
Vladi Gorovoy[1], **Subhrajit Mukherjee**[4], **Vladimir Kleiner**[1], **Ariel Ismach** ⓘ [3],
Elad Koren ⓘ [4] & **Erez Hasman** ⓘ [1]✉

Direct-bandgap transition metal dichalcogenide monolayers are appealing candidates to construct atomic-scale spin-optical light sources owing to their valley-contrasting optical selection rules. Here we report on a spin-optical monolayer laser by incorporating a WS_2 monolayer into a heterostructure microcavity supporting high-Q photonic spin-valley resonances. Inspired by the creation of valley pseudo-spins in monolayers, the spin-valley modes are generated from a photonic Rashba-type spin splitting of a bound state in the continuum, which gives rise to opposite spin-polarized $\pm K$ valleys due to emergent photonic spin–orbit interaction under inversion symmetry breaking. The Rashba monolayer laser shows intrinsic spin polarizations, high spatial and temporal coherence, and inherent symmetry-enabled robustness features, enabling valley coherence in the WS_2 monolayer upon arbitrary pump polarizations at room temperature. Our monolayer-integrated spin-valley microcavities open avenues for further classical and non-classical coherent spin-optical light sources exploring both electron and photon spins.

Light sources are indispensable components of optical systems. Thus far, various light sources of distinct statistical properties, such as super-Poissonian thermal sources[1], Poissonian laser sources[2–5] and sub-Poissonian quantum sources[6], have been investigated to cover extensive applications from classical to quantum realms. Specifically, miniaturized spin-optical light sources stand out due to great potentials in chiroptical studies and multidimensional optical communications by exploiting the additional spin degree of freedom of light[1,6]. Moreover, these spin-empowered designs offer the opportunity to interface spin-optics and spintronics for an interchange of spin information between photons and electrons to construct advanced optoelectronic devices[7]. Here the optical spin ($\sigma = \pm 1$) is associated with an intrinsic angular momentum of photons, manifested as the right-handed (σ_+) and left-handed (σ_-) circular polarizations of light.

Lifting the spin degeneracy of photonic modes or electronic transitions is a prerequisite to achieve these spin-optical light sources.

An essential way to accomplish this task is to break a structure's spatial inversion symmetry (IS); that is, the structure is non-superimposable on its space-inverted version ($\mathbf{r} \rightarrow -\mathbf{r}$ with $\mathbf{r}$ being a position vector). The introduced inversion asymmetry (IaS), together with the emergent spin–orbit interaction (SOI), results in spin-split effects in both photonic and electronic systems. For example, the photonic Rashba effect describes a momentum-space spin-split dispersion $\omega(k + \sigma\mathbf{K}_{sl})$ from an IaS photonic spin-like lattice (such as the one shown in Fig. 1a), resembling a solid-state Rashba phenomenon in which the electrons' spin-degenerate parabolic bands split into dispersions with opposite spin-polarized states under IS breaking[8–10]. Therein, the photonic SOI emerges as a spin-dependent Pancharatnam–Berry phase (geometric phase) $\phi_g(\mathbf{r}) = -2\sigma\theta(\mathbf{r})$ for the spin-flipped components of light[11,12], with $\theta(\mathbf{r})$ being the local orientation angles of the lattice sites. Moreover, these space-variant geometric phases result in a spin-dependent reciprocal lattice vector $\sigma\mathbf{K}_{sl}$ for the IaS photonic

[1]Atomic-Scale Photonics Laboratory, Russell Berrie Nanotechnology Institute, and Helen Diller Quantum Center, Technion – Israel Institute of Technology, Haifa, Israel. [2]State Key Laboratory of Advanced Optical Communication Systems and Networks, School of Physics and Astronomy, Shanghai Jiao Tong University, Shanghai, China. [3]Department of Materials Science and Engineering, Tel Aviv University, Tel Aviv, Israel. [4]Faculty of Materials Science and Engineering, Russell Berrie Nanotechnology Institute, and Helen Diller Quantum Center, Technion–Israel Institute of Technology, Haifa, Israel. ✉e-mail: mehasman@technion.ac.il
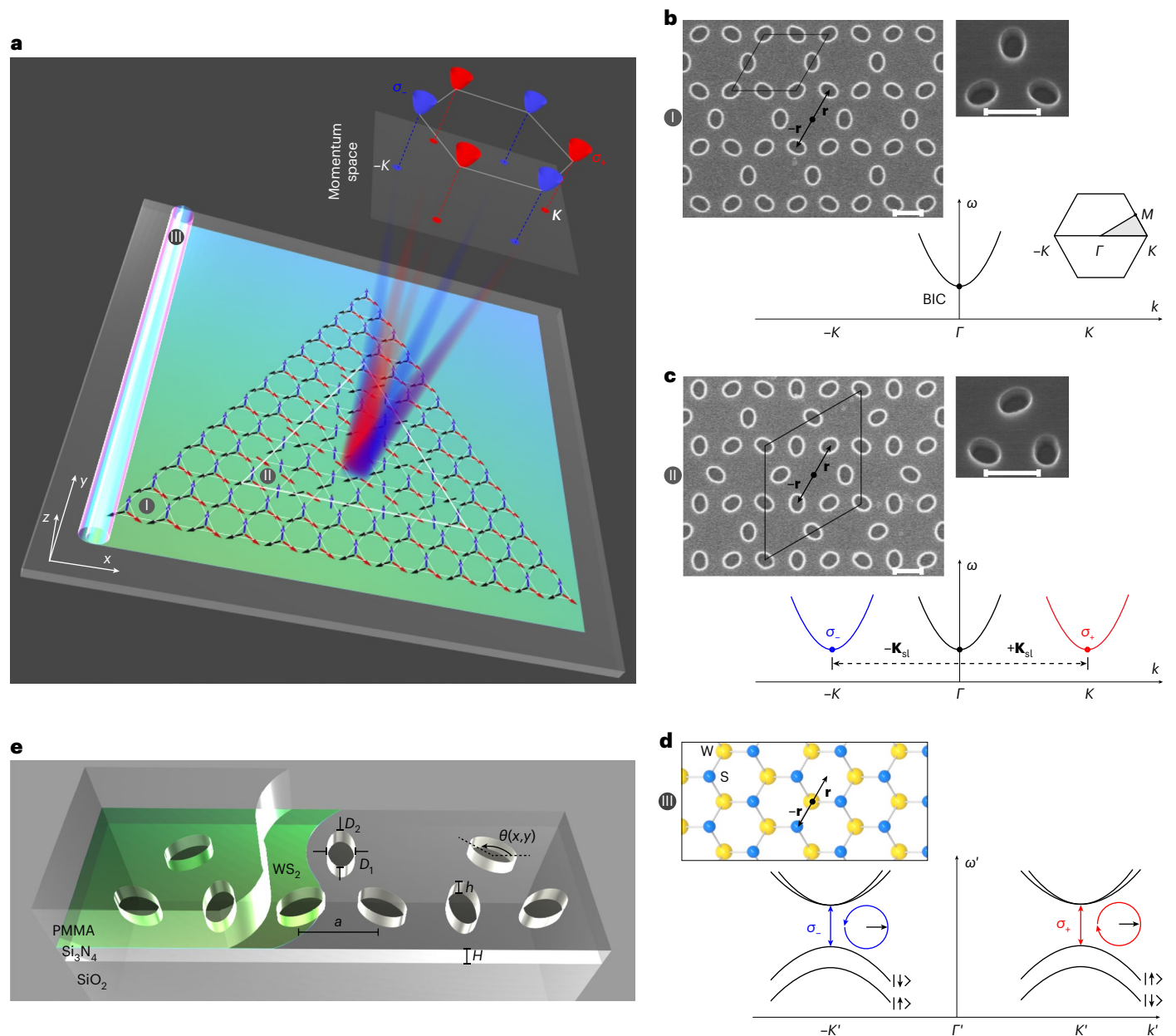
Fig. 1 | Illustration of a spin-valley Rashba monolayer laser. a, Schematic laser architecture. The spin-valley optical microcavity is constructed by interfacing a $q = 0$ (IS cladding region I) and a $q = \sqrt{3} \times \sqrt{3}$ (IaS core region II) Kagome photonic spin-like lattice. This heterostructure enables a selective lateral confinement of the $\pm K$ photonic spin-valley modes, that is, extrema of the paraboloidal band structures, inside the core for high-Q resonances, whereby coherent spin-polarized $\pm K$ lasing can be achieved from the $\pm K'$ valley excitons in an incorporated WS$_2$ monolayer (gain region III). **b**, IS photonic spin-like lattice. Top: top-view SEM image for part of the lattice and tilted-view SEM image for the constituting elliptical nanoholes. The rhombus marks a unit cell, and the two anti-parallel arrows indicate a spatial inversion transformation. Bottom: schematic band structure of the lattice highlighting the spin-degenerate

parabolic band hosting a Γ-BIC. Inset: first Brillouin zone of the lattice (unit cell shown in the top panel) labelled with high symmetry points. **c**, IaS photonic spin-like lattice. SEM images and band structure after breaking the IS of the photonic spin-like lattice shown in **b**. Due to the emergent photonic Rashba effect, the spin-degenerate parabolic band splits into two opposite spin-polarized branches, in which the $\pm K$ spin-valley modes are highlighted by red and blue dots, respectively. Scale bars, 200 nm. **d**, Valley-contrasting optical selection rules. Top: top-view cartoon for the atomic structure of a WS$_2$ monolayer. Bottom: schematic electronic band structures highlighting the valley-contrasted optical selection rules for $\pm K'$ valley excitons. **e**, Structural details in one unit cell of the IaS photonic spin-like lattice. Structural values are provided in 'Sample fabrication' in Methods.

spin-like lattice that determines the Rashba-type spin splitting, namely, $k_R = |2\mathbf{K}_{sl}|$.

Another typical electronic manifestation is the valley pseudo-spins in direct-bandgap transition metal dichalcogenide (TMD) monolayers, where broken IS leads to valley-contrasting optical selection rules for inter-band transitions at $\pm K'$ points (Fig. 1d)[13]. Consequently, TMD

monolayers are attractive active materials to construct atomic-scale spin-optical light sources, in which valley excitons (excited electron–hole pairs at $\pm K'$ valleys that radiate as in-plane $\sigma_\pm$ dipole emitters, respectively) interact with corresponding spin-polarized photonic modes for output. However, previous works were restricted by low-Q propagating chiral modes, and only incoherent (or weakly
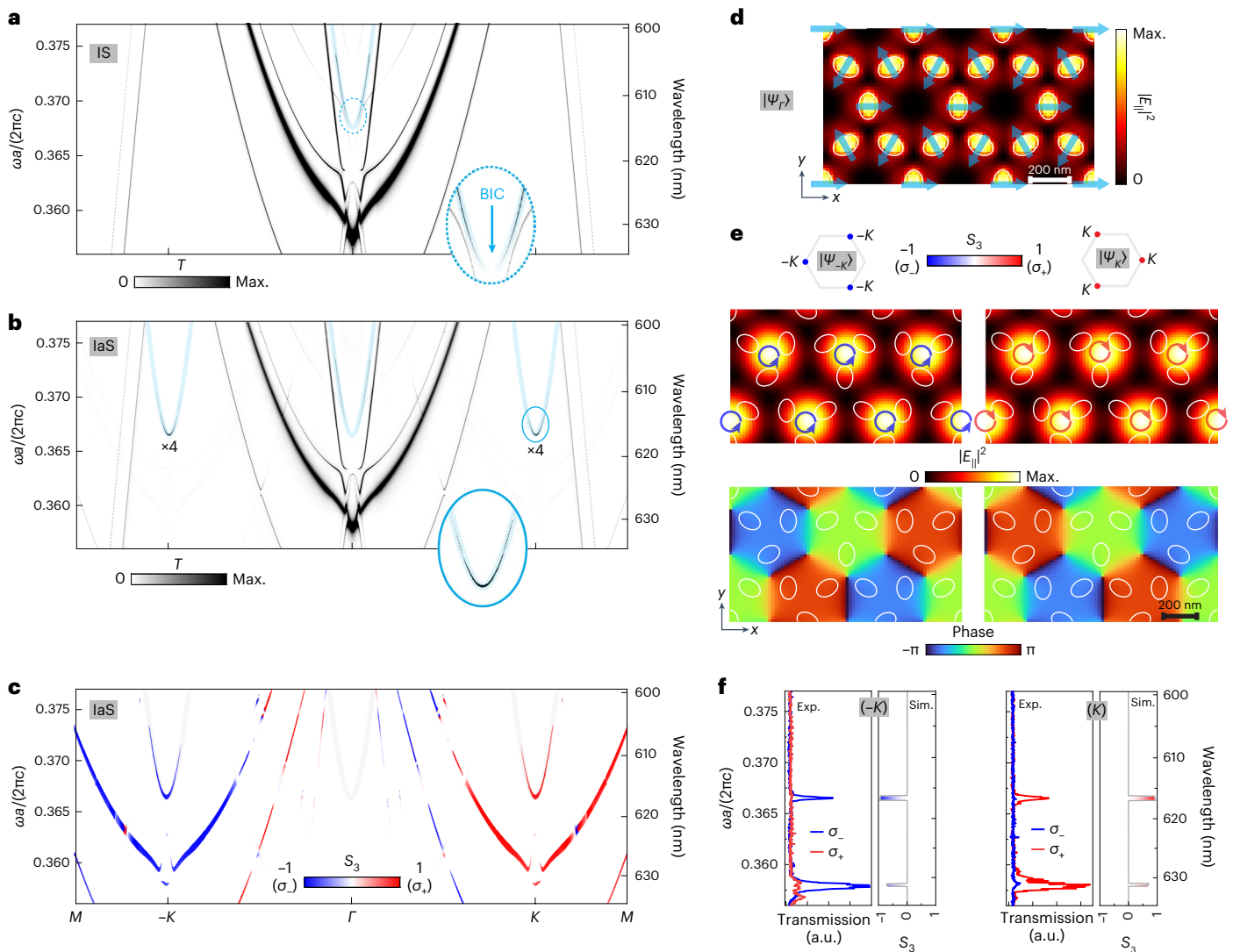
Fig. 2 | Principle of spin-valley generation via a photonic Rashba effect.
a, Calculated band structure of the periodic IS photonic spin-like lattice. A cyan curve is overlaid to highlight the parabolic band that hosts $|\Psi_\Gamma\rangle$ at the band edge. Here ω denotes the angular frequency, c denotes the speed of light in vacuum and T denotes the transmission. Max., maximum. **b**, Calculated band structure of the periodic IaS photonic spin-like lattice. Three cyan curves are overlaid to highlight those parabolic bands that host $|\Psi_\Gamma\rangle$, $|\Psi_{-K}\rangle$ and $|\Psi_K\rangle$ at the band edges. **c**, Calculated spin-polarized band structure for the periodic IaS photonic spin-like lattice. The photonic spin information is obtained by calculating the S_3 component of the Stokes vector, which describes the degree of circular polarization for each band. To highlight the differences introduced solely by the photonic Rashba effect, the same set of momentum values are used to calculate

the band structures in **a**–**c**. **d**, Simulated real-space intensity distribution of in-plane electric field for $|\Psi_\Gamma\rangle$. The white ellipses show contours of the nanoholes, in which the cyan arrows indicate the local major electric field vectors. **e**, Momentum-space spin distributions (top), real-space intensity distributions (middle) and real-space phase distributions (bottom) of in-plane electric field for $|\Psi_{-K}\rangle$ (left panels) and $|\Psi_K\rangle$ (right panels). Real-space spin distributions are overlaid by counter-clockwise (σ_-) and clockwise (σ_+) arrows. The real-space field distributions are extracted from the midplane of the Si_3N_4 film. **f**, Measured spin-resolved transmission spectra at $\pm K$ points of the IaS photonic spin-like lattice (left part of each panel). The extracted S_3 distributions (from **c**) at $\pm K$ points are also shown for comparison (right part of each panel).

coherent) additions of valley excitons' spontaneous emission were achieved[14–16], imposing undesired limitations on applications requiring both high spatial and temporal coherence.

Recently, photonic bound states in the continuum (BICs) have provoked extensive research due to merits of extremely high Q factors, which greatly facilitated light–matter interactions in lasing and nonlinear systems[17,18]. Albeit originally proposed in quantum mechanics[19], BICs are intrinsically a wave phenomenon in which a wave state resides inside the continuous spectrum of extended states but remains perfectly confined in space[20]. Typical examples include the Γ-BICs stemming from a symmetry mismatch between their near-field mode profiles and the corresponding

outgoing propagating modes in planar photonic crystal slabs[21,22]. Moreover, shaping nonradiative perfect BICs into externally accessible quasi-BICs via symmetry-broken nanostructures has been studied for practical applications, such as the tailored chiroptical responses[23–25]. However, either these demonstrations were elusive for experimental realization, or they showed an unsatisfactory trade-off between the achievable degrees of circular polarization and the Q factors for the target modes, preventing them from the construction of coherent spin-optical light sources.

Here we report on a spin-optical monolayer laser leveraging spin-valley modes, which are generated from a photonic Rashba effect by breaking the IS of a Kagome photonic crystal slab supporting a Γ-BIC
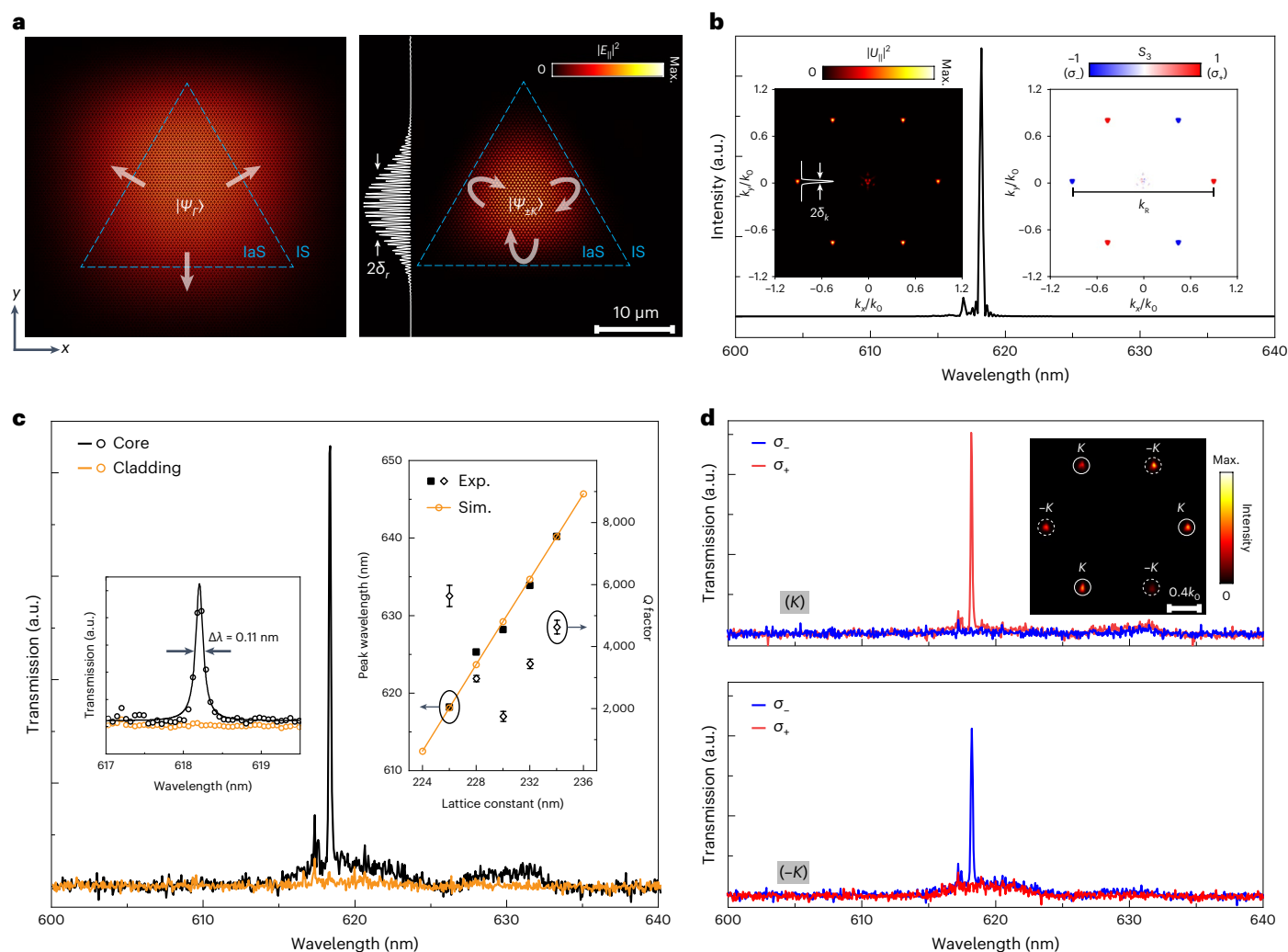
Fig. 3 | Spin-valley ('cold') optical microcavity. a, Simulated selective lateral mode confinement of $|\Psi_{\pm K}\rangle$ in the microcavity. The y-direction intensity profile of the spin-valley resonant mode (across cavity centre) is fitted by a Gaussian function with a standard deviation $\delta_r = 4.3$ μm. **b**, Calculated resonant spectrum of the microcavity. Insets: simulated momentum-space intensity and S_3 distributions of in-plane electric field for the spin-valley resonant mode. The k_y-direction intensity profile of a $-K$ spot (across spot centre) is fitted by a Gaussian function with a standard deviation $\delta_k = 0.014 k_0$ (k_0, free-space wavenumber). A product of the simulated standard deviations for the spin-valley resonant mode in momentum space and in real space satisfies a relationship: $\delta_k \times \delta_r = 0.61$. **c**, Measured transmission spectra collected from core or cladding of the microcavity. The left inset highlights the spectral region around the resonant peak, which is fitted by a Lorentz function with a linewidth $\Delta\lambda = 0.11$ nm. The right inset shows the measured peak wavelengths and Q factors of the spin-valley resonant modes in microcavities with different lattice constants. The data from a single cavity are presented for each case, and error bars are standard errors of the fitted Lorentz widths. The simulated peak wavelengths are also shown for comparison. **d**, Measured spin-resolved transmission spectra of three K emission spots and three $-K$ emission spots. The inset shows the measured momentum-space intensity distribution of the spin-valley resonant mode, where filtering pinholes (diameters of ~$0.21 k_0$) for three K spots and three $-K$ spots are indicated by solid and dashed circles, respectively. The relative intensity ratios between the emission in $\pm K$ directions and Γ direction are approximately 9.4 (**b**) and 8.6 (**d**).

(Fig. 1b). The IS breaking is introduced by controlling the orientation angles of the constituting anisotropic nanoholes according to distinct spin-like lattice configurations. This leads to a photonic Rashba-type spin splitting of the Γ-BIC into two opposite spin-polarized modes at $\pm K$ valleys, that is, $\pm K$ spin-valley modes (Fig. 1c), which offer the peculiarities of boosted spin-dependent light–matter interaction due to zero group velocities. Moreover, the spin-valley optical microcavities are constructed by interfacing two photonic spin-like lattices with IaS (core, with spin-valley modes) and IS (cladding, without spin-valley modes) properties, whereby laterally confined spin-valley resonant modes are created with high experimental Q factors ($Q_{exp.} \approx 6,000$). Consequently, coherent spin-polarized emission is achieved from $\pm K'$ valley excitons in an incorporated WS$_2$ monolayer (Fig. 1a), manifested as a quasi-single-mode Rashba monolayer laser with high spatiotemporal coherence (diffraction-limited beams) and symmetry-enabled robustness properties from the photonic spin-valley states.

Principle of photonic spin-valley generation

The planar Kagome lattices composed of elliptical nanoholes were fabricated on a Si$_3$N$_4$ film using electron-beam lithography and reactive-ion etching techniques, followed by the incorporation of a highly crystalline WS$_2$ monolayer supported by a thick poly(methyl methacrylate) (PMMA) layer[26] (Fig. 1e and 'Sample fabrication' in Methods). The Kagome lattice was chosen because of its rich geometrical frustrations of electron spins in antiferromagnets[27], leading to highly degenerate ground states with distinct chiral spin structures, such as the two typical configurations showing uniform (IS, $q = 0$) and staggered (IaS, $q = \sqrt{3} \times \sqrt{3}$) chirality distributions. Accordingly, the
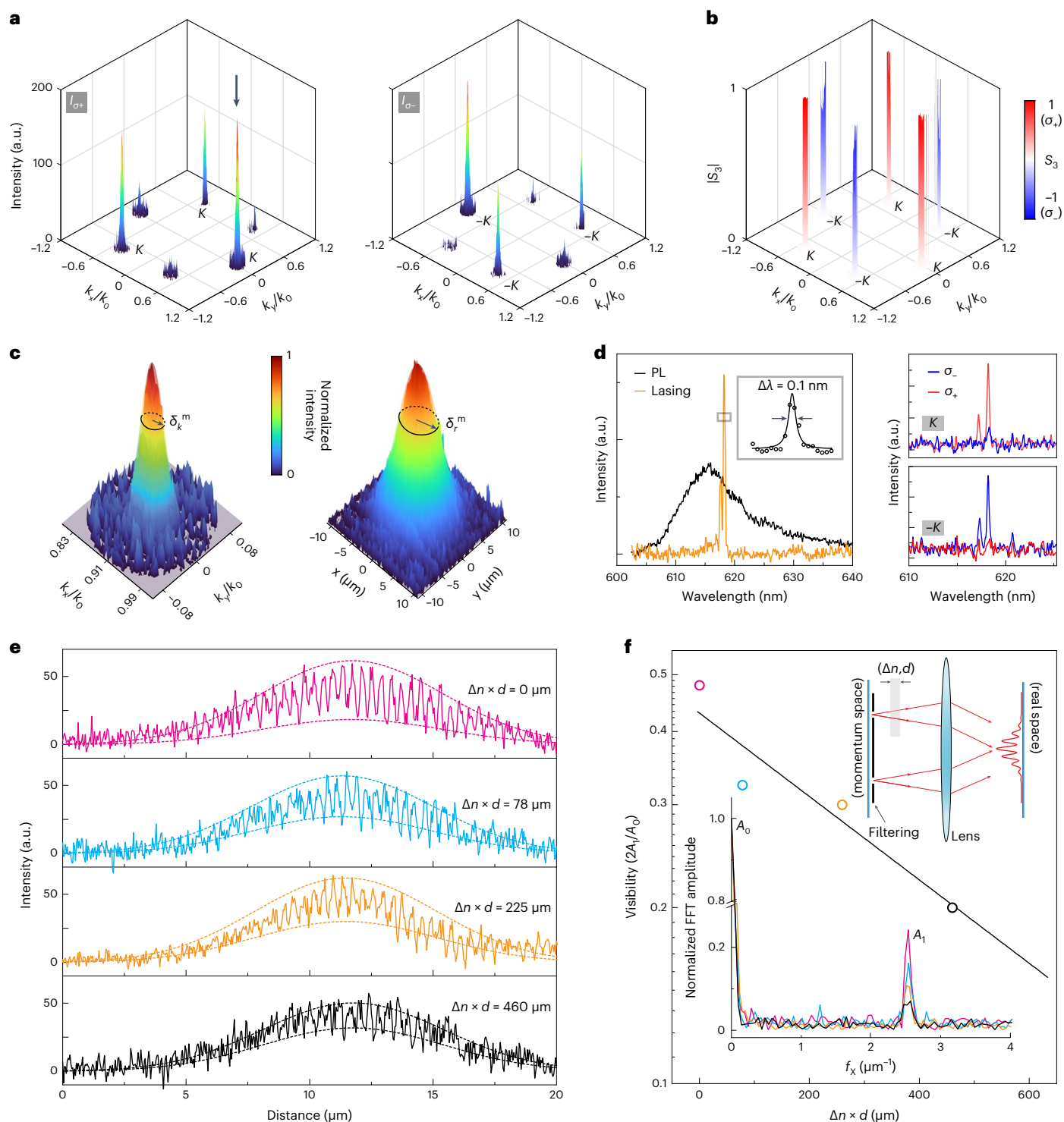
Fig. 4 | Characteristics of spin-valley Rashba monolayer lasing. a, Measured spin-dependent emission intensity distributions of the spin-valley resonant mode in momentum space. **b**, Calculated S_3 distribution based on the spin-discriminated intensity distributions shown in **a. c**, Measured intensity profiles of the spin-valley resonant mode in momentum space (left, same as the one indicated by a black arrow in **a**) and in real space (right). The two intensity profiles are fitted by two-dimensional Gaussian functions to obtain standard deviations of the resonant mode in momentum space ($\delta_k^m = 0.015k_0$) and in real space ($\delta_r^m = 3.6\,\mu m$). **d**, Left: measured emission spectra of the WS_2 monolayer outside (black) and inside (orange) the spin-valley optical microcavity from all $\pm K$ spots. Inset: detailed dominant emission peak fitted by a Lorentz function with a linewidth $\Delta\lambda = 0.10$ nm. PL, photoluminescence. Right: measured

spin-dependent emission spectra of three K spots (top) and three $-K$ spots (bottom). Note that the measured emission in Γ direction was almost suppressed to 0 due to its mode competition with $|\Psi_{\pm k}\rangle$. **e**, Measured two-beam interference fringes between two K spots under different time delays (denoted by optical path differences of $\Delta n \times d$ shown in the top inset of **f**). For each panel, the two dashed curves represent Gaussian fittings ($\delta = 3.6\,\mu m$) to the upper and lower envelops of the fringes. **f**, Measured visibility values of the interference fringes shown in **e**. The black line is a linear fitting to the decaying visibility. Top inset: schematic of the interference set-up. Bottom inset: calculated fast Fourier transform (FFT) amplitudes of different positive spatial frequencies for the interference fringes shown in **e**. The pump power for these measurements is 1,300 μW.
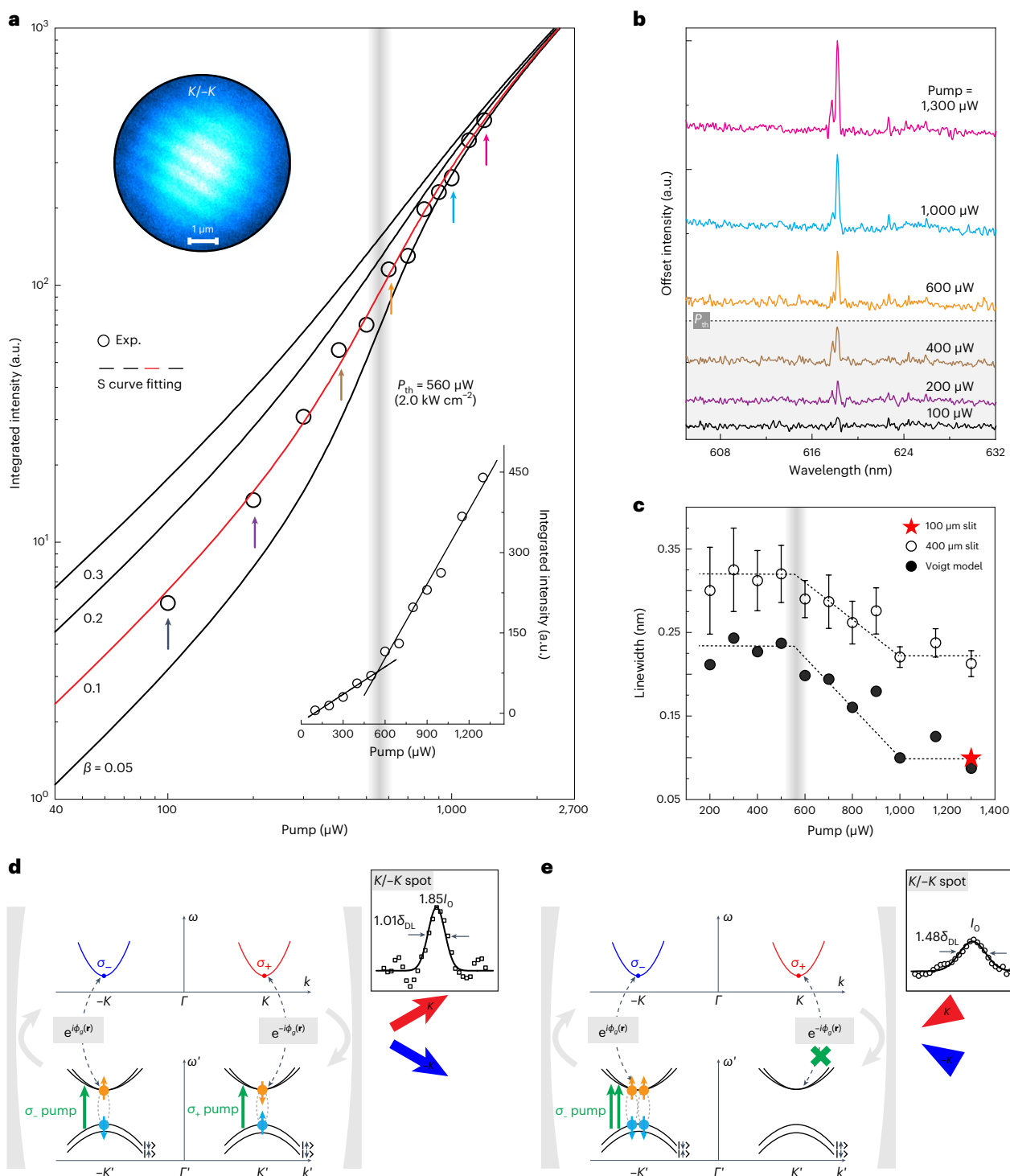
Fig. 5 | Verification of room-temperature Rashba monolayer lasing.
a, Measured output integrated intensities of the dominant emission peak as
a function of the pump power. The same intensities are plotted on a linear
scale to show the kink at the pump threshold (lower inset). The solid curves
are calculations from the laser rate equation with different β factors, and the
vertical line indicates the pump threshold. The upper inset shows the measured
interference fringes between two adjacent K and $-K$ lasing spots. **b**, Typical
emission spectra under several pump powers (indicated by colourful arrows
in **a**). Further discussion is provided in Supplementary Section 6. **c**, Measured
linewidths of the dominant emission peak as a function of the pump power.
The open circles (solid star) show the linewidths under a 400 μm (100 μm)
entrance slit width of the spectrometer, with error bars being standard errors of
the fitted Lorentz widths. The solid circles show the more accurate linewidths
retrieved from a Voigt model. The dashed black lines are a guide to the eye.

d, Minimum-loss state of Rashba monolayer laser under linear pump
polarization (with equal $\sigma_\pm$ components). The $\pm K'$ valley excitons are equally
populated and coupled with $|\Psi_{\pm K}\rangle$ for the minimum-loss state, resulting in
diffraction-limited Rashba lasing. **e**, Broken minimum-loss state of Rashba
monolayer laser under circular pump polarization. The $-K'$ valley excitons are
selectively excited via a σ_- polarized pump, which breaks the optimal minimum-
loss state (or introduces additional projection losses shown in Supplementary
Fig. 19) by suppressing the coupling between $+K'$ valley excitons and $|\Psi_K\rangle$,
resulting in degraded Rashba lasing. The inset in **d** (**e**) shows the measured cross-
section distribution of one Rashba lasing spot in momentum space under a
linearly (σ_-) polarized 532 nm pump beam. Similar results hold for a σ_+ polarized
pump. δ_{DL}, standard deviation of the corresponding diffraction-limited spot
($\delta_{DL} = 0.014k_0$); I_0, peak intensity of the spot.

orientation angles $\theta(x, y)$ of the elliptical nanoholes in the Kagome lattices were implemented following these two spin-like lattice configurations for either IS or IaS structure, as shown by the scanning electron microscopy (SEM) images in Fig. 1b,c.

The generation principle of the spin-valley modes via a photonic Rashba effect was first investigated in numerical simulations ('Numerical simulation' in Methods). Figure 2a depicts the calculated band structure for the periodic IS photonic spin-like lattice, in which the transverse-electric polarized parabolic band hosting a symmetry-protected Γ-BIC ($|\Psi_\Gamma\rangle$) is highlighted by a cyan curve. The radiationless BIC is identified by a missing transmission due to its inhibited coupling to the surrounding environment. Specifically, its vectorial field mainly distributes in the nanoholes (Fig. 2d), and hence $|\Psi_\Gamma\rangle$ can sense a strong IS breaking when the orientation angles of the nanoholes change from the $q = 0$ to the $q = \sqrt{3} \times \sqrt{3}$ configuration. To unveil the emergent spin-split effects under the broken IS, we further calculated the band structure (Fig. 2b) and the corresponding spin-resolved band structure (Fig. 2c) for the periodic IaS photonic spin-like lattice. The calculated band structures over a broader frequency range are provided in Supplementary Fig. 7. It shows that the spin-degenerate parabolic band hosting $|\Psi_\Gamma\rangle$ splits into three spin-down branches centred at $-K$ points and three spin-up branches centred at K points, manifested as a photonic Rashba effect with a spin splitting $k_R = |2\sigma\mathbf{K}_{sl}| = 4\pi/3a$. Herein, $\mathbf{K}_{sl}$ is the reciprocal lattice vector of the IaS photonic spin-like lattice; that is, $\mathbf{K}_{sl} = \frac{2\pi}{3a}\hat{\mathbf{K}}_\pm$ with $\hat{\mathbf{K}}_\pm$ being the unit vectors along Γ to K and Γ to $-K$ directions, respectively.

In particular, $|\Psi_\Gamma\rangle$ splits into one spin-down valley mode at three $-K$ points ($|\Psi_{-K}\rangle$) and one spin-up valley mode at three K points ($|\Psi_K\rangle$), whereby spin-dependent light–matter interaction can be facilitated due to their zero group velocities at the band edges. Specifically, the two spin-valley modes show inverse local spin (that is, S_3) distributions in real space (middle panels of Fig. 2e), which, in combination with the resultant opposite spin-dependent geometric phases (bottom panels of Fig. 2e), lead to their well-defined spin distributions in momentum space (top panels of Fig. 2e). These $\pm K$ spin-valley modes are achieved from a photonic Rashba effect, which thus can be further referred to as a photonic spin valley Rashba effect. Robustness analysis of the spin-valley modes under various structural parameters can be found in Supplementary Fig. 11. The generated spin-valley modes were validated by measuring the transmission spectra of a fabricated IaS photonic spin-like lattice, and the results agree with the simulations (Fig. 2f). Note that the photonic Rashba effect in this special IaS photonic spin-like lattice can be partially interpreted by conventional valley photonics. This alternative interpretation and its differences with the photonic Rashba effect are provided in Supplementary Section 4. Moreover, the uniqueness of the photonic Rashba effect is further shown by controllably changing the spin-dependent reciprocal lattice vector via versatile geometric phase designs (Supplementary Fig. 9).

Spin-valley optical microcavity

Optical microcavities are important components for intracavity mode selection and shaping, which dictate the spatiotemporal physics of lasers. In our case, heterostructures were constructed by interfacing an IaS (core) and an IS (cladding) photonic spin-like lattice to form spin-valley optical microcavities (Fig. 1a). Essentially, both the core and cladding support $|\Psi_\Gamma\rangle$, whereas only the core supports $|\Psi_{\pm K}\rangle$. This mode mismatch between core (with $|\Psi_{\pm K}\rangle$) and cladding (without $|\Psi_{\pm K}\rangle$) leads to a selective lateral confinement of the spin-valley modes inside the core for high-Q resonances ($Q_{sim.} \approx 19,000$ in simulations), namely, spin-valley resonant modes (Fig. 3a). More importantly, the heterostructure microcavity only supports a single dominant resonance locked at the wavelength of the corresponding spin-valley modes (Fig. 3b). This locking effect remains resilient against perturbations introduced by various cavity sizes, shapes and functionalities, evidencing the symmetry-enabled robustness features of the spin-valley optical

microcavities (Supplementary Section 7)[28,29]. Note that the weak side peak is a second-order transverse mode originated from the spin-valley modes as well (Supplementary Fig. 12). Consequently, the momentum space of the spin-valley resonant mode is dominated by six $\pm K$ spots, which follow an alternating spin distribution as the spin-valley modes (insets of Fig. 3b).

Experimentally, 'cold' cavity measurements were conducted to study the spin-valley resonant modes (Fig. 3c and 'Optical measurement and data analysis' in Methods). Due to a good lateral mode confinement, a narrow resonance ($\lambda = 618.2$ nm) corresponding to the spin-valley resonant mode is only observed from the core collection, in good agreement with the simulations (Fig. 3a,b). The measured linewidth of the resonance is about $\Delta\lambda = 0.11$ nm, which corresponds to a Q factor approximately $Q = \lambda/\Delta\lambda = 5,600$, being much greater than that ($Q \approx 1,600$) of a pure IaS photonic spin-like lattice without cladding (diameter ~160 μm, Fig. 2f). By simultaneously changing the lattice constants of core and cladding, wavelengths of the spin-valley resonant modes can be controlled to cover the emission wavelengths of the WS$_2$ monolayer, with a measured Q factor being generally greater than 3,000 (right inset of Fig. 3c). The fluctuated Q factors are attributed to a slightly modified optical quality of the centimetre-scale WS$_2$ monolayer during the transfer process. Moreover, we measured the spin-resolved transmission spectra for three filtered K or $-K$ spots, and the results simultaneously show a high spin polarization and a large Q factor for the spin-valley resonant mode (Fig. 3d).

Room-temperature Rashba monolayer lasing

To enable optical gain from the incorporated WS$_2$ monolayer, the core of the spin-valley microcavity was selectively pumped by a 445 nm continuous-wave laser beam with a spot standard deviation $\delta_p \approx 2.6$ μm ('Optical measurement and data analysis' in Methods). In the nonresonant pump process, it has been observed that irrespective of the polarization states of the pump, the equally populated excitons in $\pm K'$ valleys do not exhibit deterministic phase correlations. This means an absence of valley polarization and valley coherence at room temperature due to strong inter-valley scattering[30] (Supplementary Fig. 2). Those excited incoherent $\pm K'$ valley excitons will couple to the high-Q spin-valley resonant mode for optical feedback, and lasing can be realized when the achievable optical gain is higher than the system loss. Note that the WS$_2$ monolayer was chosen as the gain medium owing to its relatively high gain coefficients compared to other TMD monolayers[31], and the moderate pump spot size was adopted to match the field distribution of the spin-valley resonant mode for a higher modal gain.

Under a high pump fluence approximately $P = 4.7$ kW cm^{-2} (pump power of 1,300 μW), we first measured the spin-resolved momentum-space emission [$I_{\sigma_+}(\mathbf{k}_\parallel)$ and $I_{\sigma_-}(\mathbf{k}_\parallel)$, Fig. 4a] from the spin-valley microcavity, based on which the S_3 distribution was calculated by $S_3(\mathbf{k}_\parallel) = [I_{\sigma_+}(\mathbf{k}_\parallel) - I_{\sigma_-}(\mathbf{k}_\parallel)]/[I_{\sigma_+}(\mathbf{k}_\parallel) + I_{\sigma_-}(\mathbf{k}_\parallel)]$ (Fig. 4b). Here $\mathbf{k}_\parallel = k_x\hat{\mathbf{x}} + k_y\hat{\mathbf{y}}$ is the in-plane wavevector in momentum space ($\hat{\mathbf{x}}$ and $\hat{\mathbf{y}}$ are unit vectors in the corresponding directions). The sandwich structure, Si$_3$N$_4$/WS$_2$/PMMA, ensures a high spatial overlap (confinement factor) between the spin-valley resonant mode and the WS$_2$ monolayer, compared to the case without the PMMA encapsulation layer (Supplementary Fig. 18). This leads to an effective coupling of the excited valley excitons with the spin-valley microcavity, and highly spin-polarized directional emission is observed at $\pm K$ points (Fig. 4a,b). Specifically, the measured standard deviation of the spots is approximately $\delta_k^m = 0.015k_0$ (equivalent beam divergence half-angle of 0.86°, left panel of Fig. 4c), which corresponds to a spatial coherence length of the emission from valley excitons to be $l_{sc} = 2\pi/(2\delta_k^m) = 20.6$ μm, a value close to the measured full extension of the spin-valley resonant mode (right panel of Fig. 4c). More importantly, a product of the measured standard deviations for the spin-valley resonant mode in momentum space and in real space ($\delta_r^m = 3.6$ μm) satisfies a diffraction-limited relationship: $\delta_k^m \times \delta_r^m = 0.55$, being close to the limit (=1/2) imposed by the uncertainty

principle. Besides the tailored emission directionality, the emission spectrum of the WS$_2$ monolayer also undergoes a remarkable modification due to the presence of the spin-valley microcavity (left panel of Fig. 4d). The measured linewidth of the emergent dominant peak is approximately $\Delta\lambda = 0.10$ nm (inset of Fig. 4d), which corresponds to a temporal coherence length of the emission from valley excitons to be $l_{tc} = \lambda^2/(2\pi\Delta\lambda) = 608$ µm. Moreover, a high $\sigma_\pm$ polarization is observed for the narrow emission peak measured at $\pm K$ point (right panels of Fig. 4d), respectively, consistent with the measured spin-dependent emission intensity distributions (Fig. 4b).

In addition, two-beam interference was conducted to showcase the coherence properties of the tailored monolayer emission, as shown by the measured fringes (pink line in Fig. 4e) and visibility (pink line and circle in Fig. 4f). Details are provided in the upper inset of Fig. 4f, 'Optical measurement and data analysis' in Methods and Supplementary Section 8. As a reference, no interference fringes were observed when two background regions outside $\pm K$ spots were selected in momentum space to interfere, due to a negligible coherence of the spontaneous emission (Supplementary Fig. 16b,c). Furthermore, our interference scheme provides a convenient way to characterize the temporal coherence of the tailored monolayer emission by introducing different time delays between the two beams. The measured interference fringes for several time delays are depicted in Fig. 4e, whereby the temporal coherence length was obtained by fitting the decaying visibility to be $l_{tc} = 1/\text{slope} = 602$ µm (Fig. 4f), comparable to the value (= 608 µm) from linewidth analysis. Hence, a spin-optical monolayer light source with characteristic features of high spatial and temporal coherence was achieved from the spin-valley optical microcavity.

To verify the monolayer lasing, the pump power was varied to control the achievable optical gain from the WS$_2$ monolayer, and single dominant resonances can be observed under certain pump powers due to mode competition (Fig. 5b). Accordingly, the output intensities and linewidths of the dominant peak are calculated and shown by the open circles in Fig. 5a,c, respectively. With the growth of the input pump power, the output intensity undergoes a clear nonlinear evolution (an 'S shape' light–light curve) accompanied by a progressive linewidth narrowing, showing hallmark features of lasing around the threshold. A Voigt model was adopted to retrieve more accurate linewidths (Supplementary Section 10), which show a narrowing factor of approximately 2 to claim the lasing behaviour (solid circles in Fig. 5c)[32]. To study the threshold behaviour of miniaturized lasers, an important figure of merit is the spontaneous emission factor (β factor) that is defined as the fraction of spontaneous emission coupled into a desired lasing mode. The β factor can be evaluated by fitting the measured light–light curve using the laser rate equation (Supplementary Section 9), as shown by the solid curves in Fig. 5a. The optimal fitting gives a β factor $\beta \approx 0.1$ and a pump threshold $P_{th} = 2.0$ kW cm^{-2} (pump power of 560 µW) defined at the maximum of its first-order derivative, in good agreement with the quantum threshold analysis (Supplementary Section 9). A similar lasing was also observed from a hexagonal heterostructure microcavity, manifesting the symmetry-enabled robustness property against cavity shapes from the photonic spin-valley states (Supplementary Fig. 15). Note that a high Q factor of the spin-valley resonant mode is essential for the observation of Rashba monolayer lasing, and no lasing was observed for cavities with relatively low Q factors (that is, $Q < 2,000$). Besides, no lasing was observed when the wavelength of the spin-valley resonant mode was further away (that is, $\lambda > 635$ nm) from the exciton transition (~615 nm) of the WS$_2$ monolayer, due to an insufficient optical gain[3].

For these Rashba monolayer lasers, their intracavity spin-valley resonant modes are the coherent superposition of the two opposite spin-polarized valley modes with equal amplitudes: $|\Psi_{sl}\rangle = e^{i\phi_g(\mathbf{r})}|\Psi_{-K}\rangle + e^{-i\phi_g(\mathbf{r})}|\Psi_K\rangle$ (Supplementary Section 11). Moreover, the excited $+K'$ ($-K'$) valley excitons couple with $|\Psi_K\rangle$ ($|\Psi_{-K}\rangle$) due to a polarization matching. Consequently, driven by the lasing mechanism

to find the system's minimum-loss state[33,34], the equally populated $\pm K'$ valley excitons will also undergo a coherent superposition due to stimulated emission triggered by these intracavity modes. Specifically, the $\pm K'$ valley excitons (initially without a phase correlation) re-establish a phase-locked correlation according to the opposite geometric phases of $e^{\pm i\phi_g(\mathbf{r})}$. This leads to the establishment of valley coherence in the incorporated WS$_2$ monolayer upon arbitrary pump polarizations at room temperature (Supplementary Fig. 21a,b), as shown by the measured interference fringes between a spin-up K spot and a spin-down $-K$ spot in the upper inset of Fig. 5a.

Under circumstances that the WS$_2$ monolayer possesses a nonzero valley polarization, the minimum-loss state of the Rashba monolayer laser can be regulated to be satisfied (broken) via a linear (circular) pump polarization, offering a way to control the Rashba lasing properties (Fig. 5d,e). Experimentally, by using another more close-to-resonant continuous-wave excitation ($\lambda_p = 532$ nm) at room temperature, we measured a nonzero valley polarization (~6%; Supplementary Fig. 22) in the WS$_2$ monolayer outside of the microcavity. To demonstrate this controllability, nearly diffraction-limited $\pm K$ Rashba lasing beams were first achieved under a linear pump polarization (inset of Fig. 5d). After changing the pump to be circular polarization with the same power (inset of Fig. 5e), the Rashba lasing underwent a substantial decrease in both the spatial coherence (by 47%) and intensity (by 46%).

Conclusions

By harnessing a high-Q spin-valley resonant mode generated from a photonic Rashba effect, we reported on a spin-optical monolayer laser in a heterostructure microcavity constructed by interfacing two photonic spin-like lattices with distinct spatial inversion symmetries. The achieved lasing-mechanism-driven valley coherence in a WS$_2$ monolayer greatly relieves the previous requirements of cryogenic temperatures and linearly polarized pump beams, shedding light on more sophisticated coherent manipulations of electronic valley pseudo-spins via customized intracavity modes at room temperature. In addition to the demonstrated IaS $\sqrt{3} \times \sqrt{3}$ configuration, our design can be generalized to abundant functionalities by implementing the desired IaS arrangements of the anisotropic nanoholes for intracavity mode shaping (Supplementary Fig. 14). These achievements shall pave the way for integrated spin manipulation requiring high Q factors towards an atomic scale. Although we only show the Rashba lasing from a WS$_2$ monolayer, similar lasing can also be achieved from other gain materials due to the general photonic Rashba effect[16]. However, the realized functionality and controllability of the Rashba lasing necessitate the intrinsic valley polarizations of TMD monolayers, which are difficult to accomplish with other active materials, especially in the absence of magnetic fields at room temperature.

Inspired by the quantum entanglement achieved from an electronic Rashba effect[35], our architecture combining electronic valley pseudo-spins[36,37] and high-Q spin-valley optical microcavities offers the possibility to realize sub-Poissonian Rashba monolayer entanglement light sources, by exploring SOI of the photonic Rashba effect in a single-photon limit[6]. We envision the monolayer-integrated spin-valley optical microcavities as a multidimensional platform to study coherent spin-dependent phenomena in both classical (for example, lasing, superfluorescence, nonlinearity and polariton) and quantum (for example, single-photon sources and entanglement sources) regimes, opening new horizons in fundamental research and optoelectronic devices exploiting both electron and photon spins.

Online content

Any methods, additional references, Nature Portfolio reporting summaries, source data, extended data, supplementary information, acknowledgements, peer review information; details of author contributions and competing interests; and statements of data and code availability are available at https://doi.org/10.1038/s41563-023-01603-3.

References

1. Shitrit, N. et al. Spin-optical metamaterial route to spin-controlled photonics. *Science* **340**, 724–726 (2013).
2. Wu, S. et al. Monolayer semiconductor nanocavity lasers with ultralow thresholds. *Nature* **520**, 69–72 (2015).
3. Ye, Y. et al. Monolayer excitonic laser. *Nat. Photonics* **9**, 733–737 (2015).
4. Liu, Y. et al. Room temperature nanocavity laser with interlayer excitons in 2D heterostructures. *Sci. Adv.* **5**, eaav4506 (2019).
5. Paik, E. Y. et al. Interlayer exciton laser of extended spatial coherence in atomically thin heterostructures. *Nature* **576**, 80–84 (2019).
6. Stav, T. et al. Quantum entanglement of the spin and orbital angular momentum of photons using metamaterials. *Science* **361**, 1101–1104 (2018).
7. Sederberg, S. et al. Vectorized optoelectronic control and metrology in a semiconductor. *Nat. Photonics* **14**, 680–685 (2020).
8. Rashba, E. I. Properties of semiconductors with an extremum loop. 1. Cyclotron and combinational resonance in a magnetic field perpendicular to the plane of the loop. *Sov. Phys. Solid State* **2**, 1109–1122 (1960).
9. Ishizaka, K. et al. Giant Rashba-type spin splitting in bulk BiTeI. *Nat. Mater.* **10**, 521–526 (2011).
10. Dahan, N., Gorodetski, Y., Frischwasser, K., Kleiner, V. & Hasman, E. Geometric Doppler effect: spin-split dispersion of thermal radiation. *Phys. Rev. Lett.* **105**, 136402 (2010).
11. Berry, M. V. Quantal phase factors accompanying adiabatic changes. *Proc. R. Soc. Lond. A* **392**, 45–57 (1984).
12. Bomzon, Z., Biener, G., Kleiner, V. & Hasman, E. Space-variant Pancharatnam–Berry phase optical elements with computer-generated subwavelength gratings. *Opt. Lett.* **27**, 1141–1143 (2002).
13. Xiao, D., Liu, G.-B., Feng, W., Xu, X. & Yao, W. Coupled spin and valley physics in monolayers of MoS_2 and other group-VI dichalcogenides. *Phys. Rev. Lett.* **108**, 196802 (2012).
14. Gong, S.-H., Alpeggiani, F., Sciacca, B., Garnett, E. C. & Kuipers, L. Nanoscale chiral valley-photon interface through optical spin-orbit coupling. *Science* **359**, 443–447 (2018).
15. Sun, L. et al. Separation of valley excitons in a MoS_2 monolayer using a subwavelength asymmetric groove array. *Nat. Photonics* **13**, 180–184 (2019).
16. Rong, K. et al. Photonic Rashba effect from quantum emitters mediated by a Berry-phase defective photonic crystal. *Nat. Nanotechnol.* **15**, 927–933 (2020).
17. Kodigala, A. et al. Lasing action from photonic bound states in continuum. *Nature* **541**, 196–199 (2017).
18. Ge, X., Minkov, M., Fan, S., Li, X. & Zhou, W. Laterally confined photonic crystal surface emitting laser incorporating monolayer tungsten disulfide. *npj 2D Mater. Appl.* **3**, 16 (2019).
19. Neumann, J. V. & Wigner, E. Uber merkwürdige diskrete Eigenwerte. *Phys. Zeitschr.* **30**, 465–467 (1929).
20. Plotnik, Y. et al. Experimental observation of optical bound states in the continuum. *Phys. Rev. Lett.* **107**, 183901 (2011).
21. Fan, S. & Joannopoulos, J. D. Analysis of guided resonances in photonic crystal slabs. *Phys. Rev. B* **65**, 235112 (2002).
22. Zhen, B., Hsu, C. W., Lu, L., Stone, A. D. & Soljačić, M. Topological nature of optical bound states in the continuum. *Phys. Rev. Lett.* **113**, 257401 (2014).
23. Koshelev, K., Lepeshov, S., Liu, M., Bogdanov, A. & Kivshar, Y. Asymmetric metasurfaces with high-Q resonances governed by bound states in the continuum. *Phys. Rev. Lett.* **121**, 193903 (2018).
24. Liu, W. et al. Circularly polarized states spawning from bound states in the continuum. *Phys. Rev. Lett.* **123**, 116104 (2019).
25. Yin, X., Jin, J., Soljačić, M., Peng, C. & Zhen, B. Observation of topologically enabled unidirectional guided resonances. *Nature* **580**, 467–471 (2020).
26. Cohen, A. et al. Growth-etch metal-organic chemical vapor deposition approach of WS_2 atomic layers. *ACS Nano* **15**, 526–538 (2021).
27. Schweika, W., Valldor, M. & Lemmens, P. Approaching the ground state of the Kagomé antiferromagnet. *Phys. Rev. Lett.* **98**, 067201 (2007).
28. Ma, T. & Shvets, G. All-Si valley-Hall photonic topological insulator. *New J. Phys.* **18**, 025012 (2016).
29. Chen, X.-D., Zhao, F.-L., Chen, M. & Dong, J.-W. Valley-contrasting physics in all-dielectric photonic crystals: orbital angular momentum and topological propagation. *Phys. Rev. B* **96**, 020202 (2017).
30. Jones, A. M. et al. Optical generation of excitonic valley coherence in monolayer WSe_2. *Nat. Nanotechnol.* **8**, 634–638 (2013).
31. Lohof, F. et al. Prospects and limitations of transition metal dichalcogenide laser gain materials. *Nano Lett.* **19**, 210–217 (2019).
32. Siegman, A. E. *Lasers* (University Science Books, 1986).
33. Martin-Regalado, J., Prati, F., San Miguel, M. & Abraham, N. B. Polarization properties of vertical-cavity surface-emitting lasers. *IEEE J. Quantum Electron.* **33**, 765–783 (1997).
34. Nixon, M., Ronen, E., Friesem, A. A. & Davidson, N. Observing geometric frustration with thousands of coupled lasers. *Phys. Rev. Lett.* **110**, 184102 (2013).
35. Noguchi, R. et al. Direct mapping of spin and orbital entangled wave functions under interband spin-orbit coupling of giant Rashba spin-split surface states. *Phys. Rev. B* **95**, 041111 (2017).
36. Tokman, M., Wang, Y. & Belyanin, A. Valley entanglement of excitons in monolayers of transition-metal dichalcogenides. *Phys. Rev. B* **92**, 075409 (2015).
37. Jha, P. K., Shitrit, N., Ren, X., Wang, Y. & Zhang, X. Spontaneous exciton valley coherence in transition metal dichalcogenide monolayers interfaced with an anisotropic metasurface. *Phys. Rev. Lett.* **121**, 116102 (2018).

Methods

Sample fabrication

As schematically shown in Fig. 1e, the thickness of the silicon nitride (Si_3N_4) film is $H = 120$ nm. The short axis, major axis and depth of the elliptical nanoholes are $D_1 = 94$ nm, $D_2 = 135$ nm (ratio $e = D_1/D_2 = 0.7$) and $h = 70$ nm, respectively. The lattice constant varies from $a = 226$ nm to 234 nm to cover the largest gain region of the WS_2 monolayer ($a = 226$ nm unless otherwise stated). In the fabrication, the 120-nm-thick Si_3N_4 film was grown on a fused silica (SiO_2) substrate by low-pressure chemical vapour deposition at 600 °C. Subsequently, a 180-nm-thick PMMA (950, A4) film serving as the positive-tone electron-beam resist was spin-coated above the Si_3N_4 film (baked at 180 °C for 4 min), followed by the e-beam evaporation of a 15-nm-thick chromium (Cr) as the conductive layer. Afterwards, the PMMA film was patterned by electron-beam lithography (Raith EBPG, 100 kV) and developed in MIBK/IPA (1:3) solution for 90 s, followed by IPA and water rinse for 90 s and 120 s, respectively. These steps led to the fabrication of the desired mask on the PMMA film. Note that the thin Cr conductive layer was removed by a chromium etchant before the development process. To transfer the mask pattern to the underlying Si_3N_4 film, the reactive-ion etching was utilized to etch the uncovered Si_3N_4 film. Here the Si_3N_4 etching rate was calibrated to be 19 nm min^{-1} under a fluorine-containing gas mixture (CHF_3:SF_6:N_2 = 9:4:2), and the etching depth of $h = 70$ nm was achieved by choosing a desired etching time. Finally, the PMMA mask was fully removed by organic solvents and oxygen plasma, leaving only nanoholes upon Si_3N_4 film for next-step WS_2 monolayer transfer.

A growth-etch metal-organic chemical vapour deposition procedure was adopted to synthesize the wafer-scale continuous WS_2 monolayer that shows a comparable performance to the exfoliated ones (Supplementary Fig. 1)[26]. The highly crystalline WS_2 monolayer on a sapphire substrate was transferred via a well-established surface-energy-assisted process. A thick PMMA film (~1.2 μm) was first spin-coated above the monolayer (baked at 120 °C for 10 min) to serve as the supporting layer. In the following, the PMMA/WS_2 assembly was delaminated from the sapphire substrate by harnessing a selective water penetration along the WS_2–sapphire interface, and the centimetre-scale free-floating PMMA/WS_2 assembly was scooped out by the fabricated nanostructures under the naked eye, resulting in the final architecture of the samples after an elaborate baking process (90 °C for 30 min and 120 °C for 10 min). Note that the PMMA film plays multiple important roles in our design. In addition to a supporting layer to the WS_2 monolayer during and after the transfer process, it also serves as an encapsulation layer (for WS_2 protection and high confinement factor[3]) and an index-matching layer to the SiO_2 substrate. The schematic of the fabrication processes can be found in Supplementary Fig. 3.

Optical measurement and data analysis

All the optical measurements were conducted in ambient environment at room temperature. To measure the transmission spectra of the IaS photonic spin-like lattice (Fig. 2f) and the 'cold' cavity (Fig. 3c,d) incorporated with a WS_2 monolayer, a spatially filtered and collimated laser beam from a supercontinuum source (Fianium, SC450) was focused by a long-working distance objective (Olympus SLMPlan, ×10/NA0.25) to normally illuminate the samples from the substrate side, and the focusing spot size was controlled by varying the z location of the objective (Supplementary Fig. 4a). The forward scattered light from the nanostructures was collected by a high-numerical-aperture (NA) oil-immersion objective (Olympus PlanApo N, ×60/NA1.42) for the real-space and momentum-space processing via well-placed lenses. Specifically, the stop apertures (800-μm-diameter pinholes) were inserted at an intermediate real-space plane to select the desired structure part, such as the core or cladding selection in Fig. 3c, and the home-made pinholes (diameters of ~0.21k_0) were inserted at an intermediate momentum-space plane to filter the desired ±K spots (Supplementary Fig. 4b). To suppress the directly transmitted light, the illumination beam was set to a certain polarization state (linear or circular polarization), and only the cross-polarized scattered light was collected. Finally, the processed light was either imaged by an electron-multiplying charge-coupled device (EMCCD, Andor iXon) in momentum space or measured by a multimode fibre-connected spectrometer (Horiba, iHR320) in real space. Note that the WS_2 monolayer was well protected from the immersion oil (Thorlabs OILCL30, $n = 1.52$) by the PMMA encapsulation layer during the measurements and the oil-cleaning processes using isopropanol.

A similar set-up was used to characterize the Rashba monolayer lasing (Supplementary Fig. 5). The pump beam (linear or circular polarization) from a 445 nm continuous-wave laser (TOPTICA, 445-S) first passed through a bandpass filter and a short-pass filter to eliminate any spectral residual at the emission wavelengths of the WS_2 monolayer. The spectrally filtered pump beam was subsequently focused into a desired spot size (measured by imaging and Gaussian fitting) to excite the incorporated WS_2 monolayer from the substrate side. The excited valley excitons would interact with the resonant modes supported by the microcavities, and the scattered emission was collected by the oil-immersion objective. Here a long-pass filter (cut-off wavelength of 600 nm) was inserted when the real-space emission spectra were measured, and a bandpass filter (central wavelength of 620 nm and half-maximum bandwidth of 10 nm) was inserted when the momentum-space images were captured. Besides, a circular analyser (a quarter-wave plate followed by a linear polarizer) was used to discriminate the $\sigma_\pm$ components of the emission. To increase the experimental signal-to-noise ratio, the stop aperture was used to select the core of the microcavity, and the spatial filtering was conducted to select all the ±K spots (Fig. 4a, left panel of Fig. 4d, and Fig. 5a–c) or three K (−K) spots (right panels of Fig. 4d). The same measurement set-up was used when the pump beam was changed to be a 532 nm continuous-wave laser (Millennia Pro, Spectra-Physics).

Two different entrance slit widths (100 μm and 400 μm) of the spectrometer were used in the experiments: the former (spectral resolution of ~0.1 nm) was used for the single lasing measurements above the pump threshold (Fig. 4d), whereas the latter (spectral resolution of ~0.2 nm) was used for the light–light curve measurements (Fig. 5a). In the calculation of the momentum-space S_3 distribution (Fig. 4b), we removed a uniform background originating from both the EMCCD dark counts and the WS_2 monolayer emission without interacting with the nanostructures[16]. In the light–light curve measurements, a variable neutral density filter was used to change the pump power, which was measured by a photodiode sensor (Thorlabs, PM100D and S130C) with a power resolution of 100 pW. The pump fluence was calculated from the measured half-maximum spot diameter (~6 μm). Note that no photoluminescence was measured from other materials (SiO_2 substrate, Si_3N_4 film, PMMA layer and immersion oil) under the largest pump power in the lasing measurements.

To measure the two-beam interference (Supplementary Fig. 6), a magnification unit was added to the lasing measurement set-up, in which the fringes were magnified by an objective (Olympus SLMPlan, ×10/NA0.25) and reimaged by an EMCCD. A spatial filtering was conducted to select two ±K lasing spots in momentum space to interfere in real space. To preclude the contribution from a uniform background in momentum space, a reference interference was measured by shifting the filtering pinholes outside the ±K lasing spots (Supplementary Fig. 16b), and the difference between these two interference measurements was considered as the contribution from the Rashba monolayer lasing. To enhance the experimental signal-to-noise ratio, we averaged the intensity distribution along the direction of the emergent two-dimensional fringes. More details about the interference scheme can be found in Supplementary Section 8. In the characterization of the temporal coherence length of the Rashba monolayer lasing, glass

plates ($n = 1.46$) of different thicknesses were successively inserted after one filtered spot, which resulted in an exponential decay of the fringe visibilities due to increased time delays between the two beams. Note that the non-unity transmittance (~92%) of the glass plate has a negligible influence (<0.1% in theory) on the fringe visibility.

Numerical simulation

The simulations were implemented using a commercial finite-difference time-domain solver (Lumerical FDTD Solutions). To calculate the band structures for the periodic IS and IaS photonic spin-like lattices (Fig. 2a–c), the Bloch boundaries were used in the x and y directions, and the perfectly matched layer boundaries were used in the z direction of the corresponding unit cells. The structural parameters were set according to the description in 'Sample fabrication' in Methods. The refractive indices of SiO$_2$, Si$_3$N$_4$, PMMA and air were set to be $n = 1.46, 1.98, 1.49$ and 1.0, respectively, and no material dispersion and absorption were considered in the desired small wavelength range (610–630 nm). The spin-dependent transmission spectra $T_{\sigma_\pm}$ were calculated by illuminating the structures with broadband $\sigma_\pm$ polarized plane waves, and a spin-independent background T_{bg} resembling a Fabry–Pérot oscillation was subtracted from the calculated transmission spectra to obtain the contribution solely from the nanostructures[21], that is, $T_{\sigma_\pm} = -(T_{\sigma_\pm} - T_{bg})$. For the two band structures shown in Fig. 2a,b, the transmission was defined as $T = (T_{\sigma_+} + T_{\sigma_-})/2$. For the spin-polarized band structure shown in Fig. 2c, the S_3 values were calculated by using $S_3 = (T_{\sigma_+} - T_{\sigma_-})/(T_{\sigma_+} + T_{\sigma_-})$. Because of the coherent superposition of the two spin-valley modes (Supplementary Section 11), either K or $-K$ plane-wave incidence results in the simultaneous excitation of both spin-valley modes, and thus an inverse Fourier transform of the three K ($-K$) spots in momentum space was conducted to obtain the individual near-field distribution for $|\Psi_K\rangle$ ($|\Psi_{-K}\rangle$) (Fig. 2e).

To simulate the spin-valley resonant modes supported by the heterostructure microcavities, the perfectly matched layer boundaries were applied to all the three directions, and anti-symmetric boundaries were used in the x direction. The side length of the triangular core is 27.5 μm, and an optically thick (~12 μm) cladding is used to avoid the light penetration loss. The resonant modes were excited by a broadband in-plane linearly polarized dipole emitter located at the cavity centre, and the resonant spectra were obtained by Fourier transform of the time signals. Meanwhile, the Q factors of the desired resonant modes were obtained by fitting the decaying envelope of the time signals. The momentum-space S_3 distribution was calculated by using $S_3(\mathbf{k}_{||}) = -2\text{Im}(U_x U_y^*)/(|U_x|^2 + |U_y|^2)$, in which U_x and U_y are electric field components in momentum space, Im() refers to the calculation of the imaginary part, and the asterisk denotes the complex conjugate. The inverse Fourier transforms of specific modes in momentum space were also conducted to obtain the desired near-field distributions. Note that the WS$_2$ monolayers were ignored in these three-dimensional simulations due to a severely increased simulation time. The incorporation of the atomic-scale monolayer ($n = 5.25$)[38] mainly contributes to a slight red shift (~3.5 nm) of the resonant modes under the transparency condition.

Reporting summary

Further information on research design is available in the Nature Portfolio Reporting Summary linked to this article.

Data availability

The authors declare that the main data supporting the findings of this study are available within the article and its supplementary information. Extra data are available from the corresponding author upon reasonable request.

References

38. Jung, G.-H., Yoo, S. & Park, Q.-H. Measuring the optical permittivity of two-dimensional materials without a priori knowledge of electronic transitions. *Nanophotonics* **8**, 263–270 (2018).

Author contributions

All authors contributed significantly to this work.

Competing interests

The authors declare no competing interests.

Additional information

Supplementary information The online version contains supplementary material available at https://doi.org/10.1038/s41563-023-01603-3.

Correspondence and requests for materials should be addressed to Erez Hasman.

Peer review information *Nature Materials* thanks Alex Krasnok and the other, anonymous, reviewer(s) for their contribution to the peer review of this work.

Reprints and permissions information is available at www.nature.com/reprints.

nature research

Corresponding author(s):   Erez Hasman

Lasing Reporting Summary

Nature Research wishes to improve the reproducibility of the work that we publish. This form is intended for publication with all accepted papers reporting claims of lasing and provides structure for consistency and transparency in reporting. Some list items might not apply to an individual manuscript, but all fields must be completed for clarity.

For further information on Nature Research policies, including our data availability policy, see Authors & Referees.

▶ Experimental design

Please check: are the following details reported in the manuscript?

1. Threshold

   Plots of device output power versus pump power over a wide range of values indicating a clear threshold
   ☒ Yes ☐ No — Fig. 5a (threshold shown in both log-log and linear scale plots)

2. Linewidth narrowing

   Plots of spectral power density for the emission at pump powers below, around, and above the lasing threshold, indicating a clear linewidth narrowing at threshold
   ☒ Yes ☐ No — Fig. 5b (typical emission spectra) and Fig. 5c (linewidth narrowing factor of ~ 2)

   Resolution of the spectrometer used to make spectral measurements
   ☒ Yes ☐ No — Resolution of ~ 0.1 nm and a Voigt model was adopted to retrieve more accurate linewidth values (Supplementary text section 10)

3. Coherent emission

   Measurements of the coherence and/or polarization of the emission
   ☒ Yes ☐ No — Measurements of spatial and temporal coherence using two-beam interference (Fig. 4e,f), momentum-space imaging (Fig. 4a-c), and linewidth analysis (Fig. 4d); Measurements of spin polarizations using momentum-space imaging (Fig. 4a,b) and spectra (Fig. 4d)

4. Beam spatial profile

   Image and/or measurement of the spatial shape and profile of the emission, showing a well-defined beam above threshold
   ☒ Yes ☐ No — Measurements of well-defined beams above threshold both in momentum space and real space (Fig. 4a-c), and they satisfy a diffraction-limited relationship.

5. Operating conditions

   Description of the laser and pumping conditions
   Continuous-wave, pulsed, temperature of operation
   ☒ Yes ☐ No — Room-temperature 445-nm continuous-wave pump (measurement section in the Methods)

   Threshold values provided as density values (e.g. W cm⁻² or J cm⁻²) taking into account the area of the device
   ☒ Yes ☐ No — Fig. 5a (Pth = 2.0 kW/cm2)

6. Alternative explanations

   Reasoning as to why alternative explanations have been ruled out as responsible for the emission characteristics
   e.g. amplified spontaneous, directional scattering; modification of fluorescence spectrum by the cavity
   ☒ Yes ☐ No — We have systematically studied the spin-valley lasing modes (e.g., generation, confinement mechanism, real-space/momentum-space mode profiles, spin polarizations, topological protection properties) both in theory and in experiment, and these consistent results are shown throughout main text and Supplementary Information. The phase transition from spontaneous emission to lasing emission was further corroborated by well-defined threshold, linewidth narrowing, spatial/temporal coherence, and mode competition, which rule out other alternative explanations.

7. Theoretical analysis

   Theoretical analysis that ensures that the experimental values measured are realistic and reasonable
   e.g. laser threshold, linewidth, cavity gain-loss, efficiency
   ☒ Yes ☐ No — Simulations of lasing mode generation and properties (Figs. 2 and 3, Supplementary Figs. 11-14 and 16-20); Quantum threshold and laser rate equation analysis of the observed lasing (Supplementary text section 9)

8. Statistics

| Number of devices fabricated and tested | ☒ Yes ☐ No | We have fabricated and tested more than 50 devices with designed resonant wavelengths covering 618 nm-640 nm (Fig. 3c). Two typical lasing devices emitting around maximum gain region (~ 620 nm) are provided to demonstrate the topological protection features against cavity shape (Figs. 4 and 5, and Supplementary Fig. 15) |
| Statistical analysis of the device performance and lifetime (time to failure) | ☒ Yes ☐ No | The Rashba monolayer lasing can be achieved at the high gain region of the WS2 monolayer under a large Q-factor of the microcavity. Specifically, no lasing was observed for devices with resonant wavelengths being further away (> ~635 nm) from the exciton transition due to insufficient gain, and no lasing was observed for cavities with relatively low Q-factors (<~ 2000). The device lifetime is longer than two months. |